

# Crystalline Phases of Laser-Driven Dipolar Bose-Einstein Condensates

Chinmayee Mishra,<sup>1</sup> Stefan Ostermann,<sup>2</sup> Farokh Mivehvar,<sup>3</sup> and B. Prasanna Venkatesh<sup>1</sup>

<sup>1</sup>Indian Institute of Technology Gandhinagar, Gandhinagar 382 355, India

<sup>2</sup>Department of Physics, Harvard University, Cambridge, Massachusetts 02138, USA

<sup>3</sup>Institut für Theoretische Physik, Universität Innsbruck, Technikerstraße 21a, A-6020 Innsbruck, Austria

(Dated: July 6, 2022)

Although crystallization is a ubiquitous phenomenon in nature, crystal formation and melting still remain fascinating processes with several open questions yet to be addressed. In this work, we study the *emergent* crystallization of a laser-driven dipolar Bose-Einstein condensate due to the interplay between long-range magnetic and effectively infinite-range light-induced interactions. The competition between these two interactions results in a collective excitation spectrum with two roton minima that introduce two different length scales at which crystalline order can emerge. In addition to the formation of regular crystals with simple periodic patterns due to the softening of one of the rotons, we find that both rotons can also soften simultaneously, resulting in the formation of exotic, complex periodic or aperiodic density patterns. We also demonstrate dynamic state-preparation schemes for achieving all the found crystalline ground states for experimentally relevant and feasible parameter regimes.

**Introduction.**—Ultracold atomic gases with long-range interactions are a platform with unprecedented properties to realize exotic many-body phenomena in a well-controlled environment [1]. Long-range interactions in Bose-Einstein condensates (BECs) can either originate from the intrinsic magnetic dipole moment of atomic species [2–6], or be imposed by manipulating the BEC with external laser fields [7–12] or quantized dynamic cavity fields [13–15]. In addition to supersolid and crystalline (droplet array) phases precipitated by the long-range interactions, competition between diverse, engineered interactions in such systems can also lead to other interesting emergent physics. These include frustration in BECs confined to multi-mode cavities [16–18] and quasi-crystalline order in dipolar BECs with spin-orbit interactions [19–21] or non-dipolar BECs interacting with multiple cavities [22].

In this letter we focus on the interplay between long-ranged magnetic dipole and effectively infinite-ranged light-induced interactions in a laser-driven dipolar BEC in free space. The cigar-shaped elongated BEC is illuminated by two counterpropagating laser beams with orthogonal polarizations [see Fig. 1(a)]. On the one hand, in the absence of light this system is expected to exhibit a phase transition to supersolid [23–26] or droplet crystalline phases [27, 28]. The formation of these phases is related to the instability of a magnetic roton [29, 30] in the collective excitation spectrum of the system, similar to the one originally predicted for superfluid helium-4 [31]. On the other hand, it has been shown that for a non-dipolar BEC with imposed non-interfering, running-wave light fields the translation invariance of the system is broken, leading to the simultaneous formation of a crystalline atomic state and optical potential with an intrinsically chosen period [10–12]. This phenomenon can also be attributed to the softening of a light-induced roton mode with a wave length comparable to that of the laser field.

The fundamental question we pose in this work is: What are the phases when these two distinct interactions compete with each other? We show that this comprises an intriguing scenario which can lead to the formation of a rich variety

of crystalline and supersolid phases. We begin our analysis by calculating the collective excitation spectrum to identify the possible roton mode softening in the system. Here, we

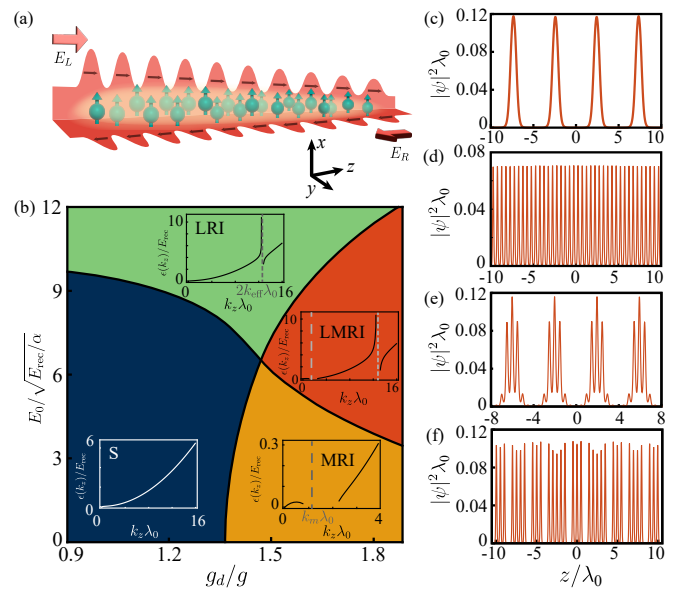


Figure 1. (Color online) (a) Schematic of a dipolar BEC in the presence of two counter-propagating laser beams of orthogonal polarisation. (b) Stability diagram of a *homogeneous* BEC as a function of dipole-interaction strength  $g_d$  and light amplitude  $E_0$  calculated from the excitation spectrum. The insets in the four regimes show examples of the typical spectrum that is stable (S) or consisting of either light (LRI) or magnetic (MRI) roton instability, or bi-roton instability (LMRI). (c-f) Atomic density patterns in the crystalline ground state phases. (c) Magnetic droplet crystal (MC) for  $\{g_d/g, \sqrt{\alpha}E_0/\sqrt{E_{rec}}\} = \{1.52, 0\}$  and (d) light crystal (LC) for  $\{g_d/g, \sqrt{\alpha}E_0/\sqrt{E_{rec}}\} = \{0.92, 12\}$ . (e-f) Light-magnetic crystal (LMC) for  $\{g_d/g, \sqrt{\alpha}E_0/\sqrt{E_{rec}}\} = \{1.42, 4.2\}$  and  $\{1.7, 5\}$ , respectively. Panel (e) corresponds to ‘droplets of supersolids’ and (f) to an aperiodic ‘crystal’. Common parameters for (b-f) include  $L = 50\lambda_0$ ,  $\omega_\rho = 100E_{rec}/\hbar$ ,  $\zeta = 0.1$ ,  $a = 70a_0$  ( $a_0$ -Bohr radius) and  $N = 10^5$  atoms.

identify regimes where the two long-range interactions compete with each other and lead to a *bi*-roton softening spectrum, indicating the existence of two possible crystallization length scales. Following this, we evaluate the ground-state phase diagram numerically and confirm the intuitive picture suggested by the excitation spectrum. Besides the two individual ordered states corresponding to each long-range interaction, we demonstrate the existence of an intertwined emergent phase with periodic or aperiodic density patterns corresponding to the bi-roton softening. Ultimately, we also outline state preparation schemes to achieve the different crystalline ground-state phases dynamically for experimentally relevant and feasible conditions.

*Model.*—We consider a trapped, driven dipolar BEC at zero temperature. The transverse harmonic trap with frequency  $\omega_\rho$  confines the BEC into a cigar shaped geometry along the  $z$ -direction [see Fig. 1(a)]. The magnetic dipoles are oriented along the  $x$ -direction. In addition, the BEC is subject to two counter-propagating, far-off resonant and orthogonally polarized (i.e., non-interfering) plane-wave laser beams. For atoms (with mass  $m$ ) in an elongated BEC confined by an axial box potential  $V_{\text{box}}(z)$  of extent  $L$ , the BEC order parameter is decomposed as  $\Psi(\mathbf{r}, t) = \psi(z, t)e^{-(\eta x^2 + y^2/\eta)/2l^2}/\sqrt{\pi l}$  where the transverse width  $l$  and transverse anisotropy  $\eta$  remain as variational parameters following the reduced 3D theory [32, 33]. The dynamics of  $\psi(z, t)$  is governed by the Gross-Pitaevskii equation extended to include quantum fluctuations given by the Lee-Huang-Yang (LHY) correction term [27, 28],

$$i\hbar \frac{\partial \psi(z, t)}{\partial t} = \left[ \mathcal{E}_\rho - \frac{\hbar^2 \nabla_z^2}{2m} + V(z) + \frac{gN}{2\pi l^2} |\psi|^2 + \Phi_\rho(z) + g_{\text{LHY}} N^{3/2} |\psi|^3 \right] \psi(z, t), \quad (1)$$

with  $\int dz |\psi(z, t)|^2 = 1$ . The variational parameters  $l$  and  $\eta$  are determined by minimizing the energy functional  $\mathcal{E}(\psi; l, \eta)$  given in the Supplement Material (SM) [34]. Here,  $\mathcal{E}_\rho = (\hbar^2/4ml^2 + ml^2\omega_\rho^2/4)(\eta + 1/\eta)$  is the transverse energy and  $g = 4\pi\hbar^2 a/m$ , with  $a$  denoting the s-wave scattering length, is the strength of two-body contact interaction. The magnitude of the LHY correction term  $\propto |\psi|^3$  is given by  $g_{\text{LHY}} = (64ga^{3/2}/15\pi^2 l^3)(1 + 3g_d^2/2g^2)$  and

$$\Phi_\rho = \frac{g_d N}{2\pi l^2} \int dk_z e^{izk_z} V_d(k_z) n(k_z), \quad (2)$$

is the dipole-dipole interaction (DDI) with  $g_d = \mu_0 d^2/3$  for atoms with a dipole moment  $d$ . Here,  $n(k_z)$  is the Fourier transform of the density and  $V_d(k_z) = [3(1 - q^2 e^{q^2} \Gamma[0, q^2])/(1 + \eta) - 1]$  with  $q = k_z^2 l^2 \sqrt{\eta}/2$  and  $\Gamma[a, b]$  denoting the incomplete Gamma function.

The potential  $V(z)$  in Eq. (1) consists of the box potential,  $V_{\text{box}}(z) = 0$  if  $|z| \leq L/2$ , else  $\infty$ , and the optical potential  $V_{\text{opt}}(z)$  induced by the incoming light beams, i.e.,  $V(z) = V_{\text{box}}(z) + V_{\text{opt}}(z)$ . Since the incoming left  $E_L(z)$  and right  $E_R(z)$  propagating laser fields are assumed to be orthogonally polarized, no interference occurs between them and the

optical potential depends only on the sum of the individual intensity distributions as  $V_{\text{opt}}(z) = -\alpha(|E_L(z)|^2 + |E_R(z)|^2)$ , with  $\alpha$  denoting the real part of the polarizability of the atoms. The laser fields individually satisfy the Helmholtz equation with the atomic density acting as a refractive medium,

$$\frac{\partial^2}{\partial z^2} E_{L,R}(z) + \frac{(2\pi)^2}{\lambda_0^2} \left[ 1 + \zeta \lambda_0 |\psi(z, t)|^2 \right] E_{L,R}(z) = 0, \quad (3)$$

subject to the boundary conditions described in SM [34]. Here,  $\lambda_0 = 2\pi/k_0$  denotes the wavelength of the incoming plane-wave laser field. The dimensionless quantity  $\zeta = \alpha N/2\pi\epsilon_0 l^2 \lambda_0$  characterizes the coupling between the atomic density and the light. Note that for running-wave laser fields in the absence of the atomic back-action,  $V_{\text{opt}}(z)$  amounts simply to a position-independent constant energy shift.

*Collective excitations and instabilities of a homogeneous condensate.*—As a first step to understand the nature of the ground states of the coupled Eqs. (1) and (3) in the absence of  $V_{\text{box}}$ , we analyze the collective excitation spectrum of the system by linearizing the equations of motion about a homogeneous atomic wavefunction  $\psi_0(z) = 1/\sqrt{L}$  and plane-wave fields  $E_{L,R}^0(z) = E_0 e^{\pm i k_{\text{eff}} z}$  with  $E_0$  denoting the amplitude of the driving laser fields far away from the BEC. The resulting dispersion relation reads,

$$\epsilon(k_z) = \left[ \frac{\hbar^2 k_z^2}{2m} \left\{ \frac{\hbar^2 k_z^2}{2m} + \frac{gN}{\pi l^2 L} + \frac{g_d N}{\pi l^2 L} V_d(k_z) + \frac{3g_{\text{LHY}} N^{3/2}}{L^{3/2}} \right. \right. \\ \left. \left. - \frac{32\pi^2 \zeta \alpha |E_0|^2}{L \lambda_0 (k_z^2 - 4k_{\text{eff}}^2)} \right\} \right]^{1/2}, \quad (4)$$

with the effective propagation wavenumber  $k_{\text{eff}} = (2\pi/\lambda_0) \sqrt{1 + \zeta \lambda_0 |\psi_0|^2}$  of light in the homogeneous atomic cloud. Clearly the spectrum has features from both the magnetic DDI and light-induced interactions (LII).

We analyze the collective-excitation spectrum (4) with respect to the strength of magnetic dipole interaction  $g_d/g$  and the amplitude of the light fields  $E_0$  [35]. In Fig. 1(b), we show the three distinct types of collective instabilities [ $\epsilon^2(k_z) < 0$ ] which can occur in this system. Insets in Fig. 1(b) show the representative spectrum for each parameter region. For the parameters chosen in Fig. 1(b) we see that for a fixed small value of  $\sqrt{\alpha} E_0 / \sqrt{E_{\text{rec}}} \lesssim 6$  the system develops a magnetic roton as  $g_d/g$  is increased. This roton eventually softens at the wavenumber  $k_m$ , signaling a transition from the stable (S) regime to the magnetic roton instability (MRI) regime [29]. In the same vein, tuning  $E_0$  at a fixed and sufficiently small  $g_d/g \lesssim 1.3$  leads to a roton induced by the light fields. This roton eventually softens at  $2k_{\text{eff}}$  and the system enters into the light roton instability (LRI) regime [10].

In addition to these expected instabilities where one of the two long-range interaction is dominant, we also find a third type of instability when both  $g_d/g$  and  $E_0$  are increased in order to enter a *bi*-roton instability (LMRI) region. Here, the magnetic and the light-induced rotons are simultaneously unstable. As we discuss later, contributions from both wavenumbers  $k_m$  as well as  $2k_{\text{eff}}$  ( $> k_m$ ) give rise to a new phase with

periodic or aperiodic density patterns. Moreover, the non-linearity of the phase boundaries in Fig. 1(b) clearly shows the interplay between the rotons. The S-LRI and MRI-LMRI transition boundaries are significantly altered when  $g_d/g$  is increased as the nonlinear dependence of DDI on  $k_z$  helps soften the higher momentum modes and lower the critical  $E_0$  needed to instigate the transition. Alternately, an increase in  $E_0$  pushes the S-MRI and LRI-LMRI transition boundaries to higher  $g_d/g$  values as the light fields counteract the unstable magnetic roton and cure it. This can be well understood by the low momentum behaviour of the spectrum  $\epsilon(k_z \ll 2k_{\text{eff}})$  where the last term in Eq. (4) becomes dominantly positive requiring higher magnitude of  $g_d/g$  for magnetic roton softening. An important distinction between the two rotons is their instability width over the momentum axis. While LRI remains sharply peaked at  $2k_{\text{eff}}$ , the MRI can span over a broad range of momenta. This greatly influences the density distribution of the corresponding stable ground states.

*Periodic and aperiodic crystallization.*—In order to obtain the density-wave ground states precipitated from the various roton instabilities in the excitation spectrum, we look for the stationary states of the system in a finite size box potential. We employ imaginary time evolution and conjugate gradient methods [36, 37] along with a fourth-order Runge-Kutta method to simultaneously solve the eGPE and the Helmholtz equation, Eqs. (1) and (3). Deep in the MRI and the LRI regimes a straight-forward mapping exists to the stationary states of the magnetic crystal/droplet (MC) [see Fig. 1(c)] [29] and light crystal/droplet (LC) [see Fig. 1(d)] [10] phases, respectively. The periodicity of these density patterns for the MC (LC) is set by the softened momenta associated with the magnetic (light) roton.

Apart from these two known phases, the bi-roton instability found in this system engenders peculiar light-magnetic crystal (LMC) states, where the two long-range interactions compete with one another. This competition can either result in density waves with periodic or aperiodic order [see Fig. 1(e,f)] [38]. Fig. 1(e) shows an example of the former. The density exhibits a periodic envelope of droplets (induced by the DDI) where each of them support intra-droplet crystals (set by the LII) of smaller periodicity, thus forming a unique ‘droplets of super-solids’ state. Note that the parameters  $g_d/g = 1.42$ ,  $\sqrt{\alpha}E_0 = 4.2\sqrt{E_{\text{rec}}}$  used for Fig. 1(e) indicate that the LII effects are prominent even below the LMRI threshold in Fig. 1(b) due to finite-size effects to be discussed in the following section. This is in contrast to the aperiodic ordered pattern in Fig. 1(f) that is observed for higher  $E_0$  values away from the MRI-LMRI boundary. The lack of discrete translational symmetry in such structures can be attributed to contributions from a broad range of momenta associated with the softened magnetic roton. Furthermore, note that the emergence of atomic density patterns shown in Figs. 1(d-f) is accompanied by the development of a standing-wave light field [10] (see [34]).

*Phase diagram.*—The biggest challenge in determining the numerical phase diagram of this system is the highly non-convex nature of the energy landscape in the regimes with

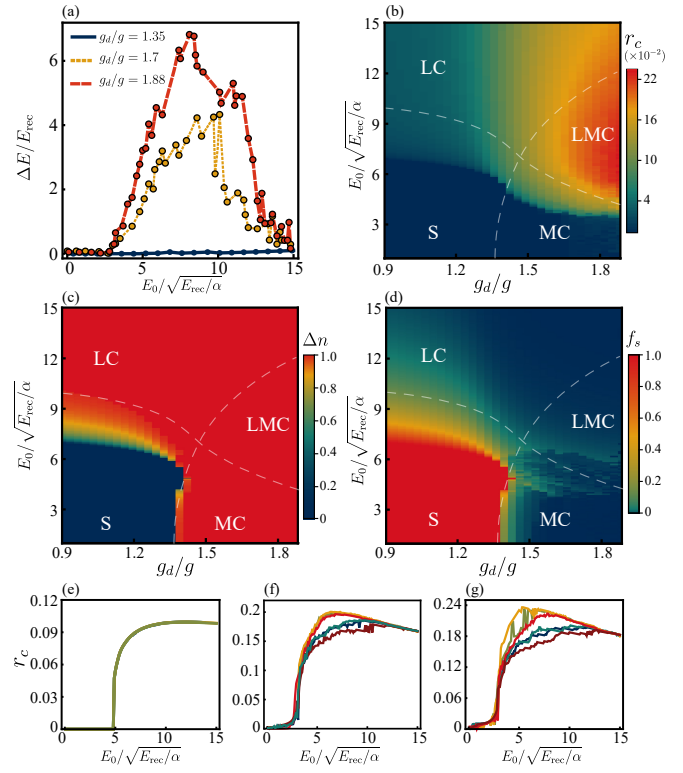


Figure 2. (a). Maximum energy difference between converged states of the eGPE for six different initial guesses for three  $g_d/g$  values. (b-d). Mean-field phase diagram as a function of  $\{g_d/g, \sqrt{\alpha}E_0 / \sqrt{E_{\text{rec}}}\}$  characterized by reflection coefficient  $r_c$  (b), density contrast  $\Delta n$  (c), and superfluid fraction  $f_s$  (d). White dashed lines are the stability diagram boundaries from the excitation spectrum. (e-f). Reflection coefficients for converged states of eGPE obtained from different initial guesses for  $g_d/g = 1.35$  (e), 1.7 (f) and 1.88 (g). All other parameters are the same as Fig. 1(b).

strong DDI, where the simulations converge to different local minima for different initial guesses irrespective of the numerical methods used. For purely magnetic crystals this is easily taken care of by starting from different multi-Gaussian ansatzes and comparing their final energies [39]. However, when the applied light fields  $E_0$  are also increased, not only the energetically dense local minima are potentially numerous but also the choice of initial guesses is no longer obvious. Therefore, convergence to the true global minimum remains ambiguous. In Fig. 2(d) we parameterize the non-convexity of the energy landscape via the maximum energy difference  $\Delta E$  obtained from different initial ansatzes. Deviation of  $\Delta E$  from zero indicates that the converged solutions are ‘quasi-stationary’ states, associated with different local minima. The recovery of convexity in the energy landscape for high  $E_0$  can be intuitively attributed to the ‘curing’ of unstable magnetic roton due to increasing LII.

Interestingly, the non-convexity does not hinder the detection of the phase boundaries as the qualitative nature of the density patterns obtained from all initial guesses remains similar [34]. In order to obtain the structural transition bound-

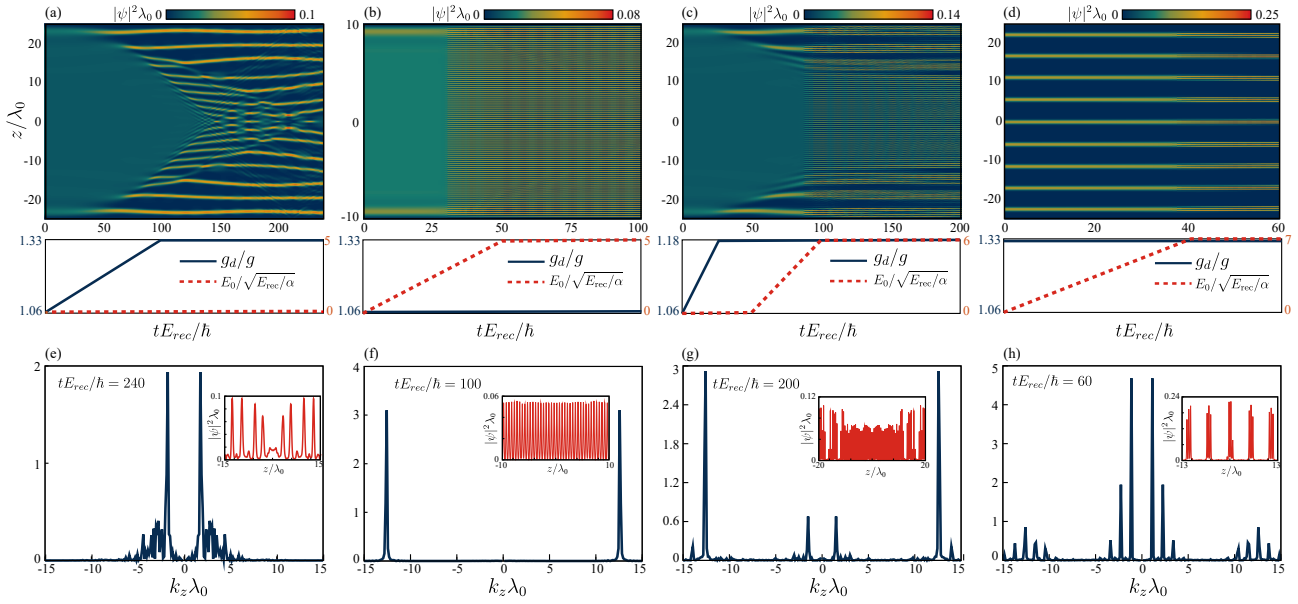


Figure 3. Preparation of (a) magnetic crystal (MC), (b) light crystal (LC), and (c) light-magnetic crystal (LMC) states starting from an unordered state, and (d) LMC starting from a MC for Dy atoms with their corresponding ramping schemes of  $g_d/g$  and the light intensities  $E_0$  shown in the middle row. The bottom row (e-h) depicts the corresponding densities in momentum space at the final time. For concreteness, the final-time density distributions in real space are shown in the insets. All other parameters are the same as Fig. 1(b).

aries we focus on three key observables—namely, the reflection coefficient  $r_c$  (defined in SM [34]) which measures the back-reflection of the incoming light fields due to the dynamic formation of a density grating, the density contrast  $\Delta n = |n_{\max} - n_{\min}|/(n_{\max} + n_{\min})$  in the bulk of the condensate, and the superfluid fraction  $f_s = (L/n)(\int |\psi|^2 dz)^{-1}$  [33, 40, 41]. By determining these quantities in the parameter space of  $g_d$  and  $E_0$  as in Fig. 1, we obtain the mean-field phase diagrams of the system shown in Fig. 2.

The reflection coefficient  $r_c$  acts as a robust parameter to detect the onset of dominant light effects and in general is also a non-destructive experimental probe of the emergent light crystalline order. Although the excitation spectrum boundaries are in qualitative agreement with the numerical simulations, the influence of the box-potential-induced edge effects lowers the light intensity threshold at which LII effects can become prominent as seen in Fig. 2(b). The threshold is further lowered at  $g_d/g \gtrsim 1.35$  when magnetic crystallization leads to increasingly denser droplets. A stronger dipole moment not only reduces the transition threshold but also steepens the structural transition curve with respect to  $E_0$ . The  $r_c$  increases with increasing DDI due to the formation of denser droplets making the medium more opaque. The contrast  $\Delta n$  is used to faithfully mark any transition from the unordered state to the crystalline phases and varies smoothly across the crystalline phases; see Fig. 2(c).

Finally, the superfluid fraction  $f_s$  shown in Fig. 2(d) reduces as  $g_d/g$  increases for any fixed  $E_0$  in LC and LMC phases. For  $g_d/g \gtrsim 1.5$ , there is a visible recovery of the superfluidity as one enters the LMC phase from MC accompanied by the emergence of the peculiar droplet of supersolid states. Clearly,

light-induced interactions play a significant role in enhancing the supersolid properties. The non-convexity of the energy landscape is also seen via  $r_c$  [see Fig. 2(e-g)] which shows oscillations in the same region with  $\Delta E \neq 0$  indicating the ‘curing’ of the MRI due to the LII for higher  $E_0$  values.

*State preparation and dynamics.*—Finally, we demonstrate in Fig. 3 that despite the non-convexity of the energy landscape all crystalline states (LC, MC, LMC) of the phase diagram can be prepared dynamically. This is in contrast to a recent work where the combination of non-convexity and symmetry leads to amorphous behaviour for a self-organized BEC in a cavity with Rydberg-excitation-induced long-range interactions [42]. For the experimentally relevant  $d = 10\mu_B$  (corresponding to Dy atoms) and  $\omega_\rho/2\pi = 100$  Hz, beginning with a uniform bulk condensate at high scattering length  $a = 100a_0$  in the absence of light fields the three different crystal phases are obtained by either quenching  $g_d/g$  (by varying  $a$ ) or ramping  $E_0$  up from zero in a box trap. The corresponding sweeping schemes are plotted in the second row of Fig. 3.

The dynamics reveal several crucial distinctions between the emergence of the MC [Fig. 3(a)] vs the LC [Fig. 3(b)]. In the MC phase within a box trap, the crystalline order sets in locally from the edges [43] and grows towards the center. While in LC, the onset of order is sharp and global. The MC excitation due to the sweeping involves both lattice vibrations and amplitude oscillations. In contrast, the phononic modes are almost frozen for the LC once it sets in. This pinning effect is a by-product of the singularly dominant momentum peaks at  $\pm 2k_{\text{eff}}$  as well as the light-field boundary conditions. During the emergence of the LMC phase [see Fig. 3(c)] both these behaviors are observed as  $g_d/g$  and  $E_0$  are swept sequentially

with a holding time in between.

Interestingly, depending on the holding time after  $g_d/g$  is quenched and before  $E_0$  is ramped, very different LMC density patterns can be obtained due to the pinning effect. In Fig. 3(d) the MC is chosen as the initial state, as opposed to the homogeneous state in Figs. 3(a,b,c). This provides a greater control over the desired LMC state. For example, the droplets of supersolid state can be prepared by ramping  $E_0$  which allows the deterministic manipulation of the intra-droplet contrast. The momentum space distribution and spatial patterns (inset) of the densities at final times are illustrated in the bottom row of Fig. 3. A visual comparison between Fig. 3(e) and (f) clearly shows that the fat-tailed distribution in case of the MC correlates with the ‘softness’ of the crystalline order while the single peak corresponding to the LC indicates the ‘stiffness’ of the spatially pinned LC [44].

*Conclusions and outlook.*— In conclusion, we have demonstrated that competing long-range interactions in a laser-driven dipolar BEC can lead to a rich phase diagram with a variety of crystalline phases. While we have been careful to restrict ourselves to experimentally relevant system parameters, an important challenge to realize the predicted crystalline structures is to minimize the laser-induced heating rate which scales as  $R \sim (\Gamma^3/8\Delta_a^2)(I/I_{\text{sat}})$  for an optical transition with linewidth  $\Gamma$ , detuning  $\Delta_a$ , saturation intensity  $I_{\text{sat}}$  and laser intensity  $I = c\epsilon|E_0|^2/2$ . We show in detail in SM [34] that this heating rate takes manageable values in state-of-the-art setups with Erbium or Dysprosium (Dy) BECs. For instance, the 741 nm transition of Dy with  $\Gamma = 2\pi \times 1.8$  KHz, with a laser intensity  $I = 0.6$  W/cm<sup>2</sup>, and detuning  $\Delta_a = 2\pi \times 1.6$  MHz leads to  $R \sim 34$  Hz. Comparing this to our state preparation time scales of  $\sim 100\hbar/E_{\text{rec}}$ , it becomes clear that the phases we predict are achievable in current experimental setups.

At a wider level, our work opens up a promising direction for next generation experiments and theoretical studies involving dipolar BECs where the addition of a laser drive leads to fascinating phenomena. Some pertinent follow-up questions include a detailed understanding of the nature of the phase transitions by taking the appropriate thermodynamic limit [45], unequivocal demonstration (beyond the heuristic superfluid-fraction measure) of the restoration of phase coherence in magnetic droplet crystals due to the driving lasers and the formation of LMC phase, and the impact of harmonic trapping along the axial  $z$  direction. We will address some of these in a forthcoming work [46].

C. M. acknowledges support from IIT Gandhinagar via the Early Career Fellowship program. S. O. is supported by a postdoctoral fellowship of the Max Planck Harvard Research Center for Quantum Optics. F. M. acknowledges financial supports from the Stand-alone project P 35891-N of the Austrian Science Fund (FWF), and the FET Network Cryst3 funded by the European Union (EU) via Horizon 2020. F. M. and B. P. V. acknowledge support from an India-Austria DST-BMWF joint project with the project numbers IN 05/2020 and DST/INT/BMWF/AUSTRIA/P-06/2020, respectively.

---

- [1] N. Defenu, T. Donner, T. Macrì, G. Pagano, S. Ruffo, and A. Trombettoni, (2021), [arXiv:2109.01063](https://arxiv.org/abs/2109.01063).
- [2] L. Santos, G. V. Shlyapnikov, P. Zoller, and M. Lewenstein, *Phys. Rev. Lett.* **85**, 1791 (2000).
- [3] T. Lahaye, C. Menotti, L. Santos, M. Lewenstein, and T. Pfau, *Reports on Progress in Physics* **72**, 126401 (2009).
- [4] M. A. Baranov, M. Dalmonte, G. Pupillo, and P. Zoller, *Chemical Reviews* **112**, 5012 (2012).
- [5] M. A. Norcia and F. Ferlaino, *Nature Physics* **17**, 1349 (2021).
- [6] L. Chomaz, I. Ferrier-Barbut, F. Ferlaino, B. Laburthe-Tolra, B. L. Lev, and T. Pfau, (2022), [arXiv:2201.02672](https://arxiv.org/abs/2201.02672).
- [7] S. Giovanazzi, D. O’Dell, and G. Kurizki, *Phys. Rev. Lett.* **88**, 130402 (2002).
- [8] D. H. J. O’Dell, S. Giovanazzi, and G. Kurizki, *Phys. Rev. Lett.* **90**, 110402 (2003).
- [9] J. Honer, H. Weimer, T. Pfau, and H. P. Büchler, *Phys. Rev. Lett.* **105**, 160404 (2010).
- [10] S. Ostermann, F. Piazza, and H. Ritsch, *Phys. Rev. X* **6**, 021026 (2016).
- [11] S. Ostermann, F. Piazza, and H. Ritsch, *New Journal of Physics* **19**, 125002 (2017).
- [12] I. Dimitrova, W. Lunden, J. Amato-Grill, N. Jepsen, Y. Yu, M. Messer, T. Rigaldo, G. Puentes, D. Weld, and W. Ketterle, *Phys. Rev. A* **96**, 051603 (2017).
- [13] R. Mottl, F. Brennecke, K. Baumann, R. Landig, T. Donner, and T. Esslinger, *Science* **336**, 1570 (2012).
- [14] H. Ritsch, P. Domokos, F. Brennecke, and T. Esslinger, *Rev. Mod. Phys.* **85**, 553 (2013).
- [15] F. Mivehvar, F. Piazza, T. Donner, and H. Ritsch, *Advances in Physics* **70**, 1 (2021).
- [16] S. Gopalakrishnan, B. L. Lev, and P. M. Goldbart, *Nature Physics* **5**, 845 (2009).
- [17] A. J. Kollár, A. T. Papageorge, V. D. Vaidya, Y. Guo, J. Keeling, and B. L. Lev, *Nature Communications* **8**, 14386 (2017).
- [18] V. D. Vaidya, Y. Guo, R. M. Kroese, K. E. Ballantine, A. J. Kollár, J. Keeling, and B. L. Lev, *Phys. Rev. X* **8**, 011002 (2018).
- [19] Y. Deng, J. Cheng, H. Jing, C.-P. Sun, and S. Yi, *Phys. Rev. Lett.* **108**, 125301 (2012).
- [20] S. Gopalakrishnan, I. Martin, and E. A. Demler, *Phys. Rev. Lett.* **111**, 185304 (2013).
- [21] X. Li, Q. Wang, H. Wang, C. Shi, M. Jardine, and L. Wen, *Journal of Physics B: Atomic, Molecular and Optical Physics* **52**, 155302 (2019).
- [22] F. Mivehvar, H. Ritsch, and F. Piazza, *Phys. Rev. Lett.* **123**, 210604 (2019).
- [23] L. Chomaz, D. Petter, P. Ilzhöfer, G. Natale, A. Trautmann, C. Politi, G. Durastante, R. M. W. van Bijnen, A. Patscheider, M. Sohmen, M. J. Mark, and F. Ferlaino, *Phys. Rev. X* **9**, 021012 (2019).
- [24] F. Böttcher, J.-N. Schmidt, M. Wenzel, J. Hertkorn, M. Guo, T. Langen, and T. Pfau, *Phys. Rev. X* **9**, 011051 (2019).
- [25] M. Guo, F. Böttcher, J. Hertkorn, J.-N. Schmidt, M. Wenzel, H. P. Büchler, T. Langen, and T. Pfau, *Nature* **574**, 386 (2019).
- [26] L. Tanzi, E. Lucioni, F. Famà, J. Catani, A. Fioretti, C. Gabbanini, R. N. Bisset, L. Santos, and G. Modugno, *Phys. Rev. Lett.* **122**, 130405 (2019).
- [27] F. Wächtler and L. Santos, *Phys. Rev. A* **94**, 043618 (2016).
- [28] R. N. Bisset, R. M. Wilson, D. Baillie, and P. B. Blakie, *Phys. Rev. A* **94**, 033619 (2016).
- [29] L. Chomaz, R. M. W. van Bijnen, D. Petter, G. Faraoni,

S. Baier, J. H. Becher, M. J. Mark, F. Wächtler, L. Santos, and F. Ferlaino, *Nature Physics* **14**, 442 (2018).

[30] G. Natale, R. M. W. van Bijnen, A. Patscheider, D. Petter, M. J. Mark, L. Chomaz, and F. Ferlaino, *Phys. Rev. Lett.* **123**, 050402 (2019).

[31] L. Landau, *Phys. Rev.* **60**, 356 (1941).

[32] P. B. Blakie, D. Baillie, and S. Pal, *Communications in Theoretical Physics* **72**, 085501 (2020).

[33] P. B. Blakie, D. Baillie, L. Chomaz, and F. Ferlaino, *Phys. Rev. Research* **2**, 043318 (2020).

[34] See Supplemental Material for details regarding the solution of the Helmholtz equation, calculation of the excitation spectrum, initial guesses for the ground state calculation of eGPE, electric field profiles obtained in the LC and LMC regimes, and heating rate calculations.

[35] Note that in Fig. 1 and Fig. 2  $g_d/g$  is varied by modifying the dipole moment over the range  $7 < d/\mu_B < 10$  while holding  $a$  constant. Though not realistic from an experimental point of view, this helps in a direct comparison of the interplay purely between the two long-range interactions. Nonetheless, it is conceivable that every point on the phase diagrams can also be attained by varying  $a$  for the fixed values of  $d = 7\mu_B$  [Erbium] and  $d = 10\mu_B$  [Dysprosium (Dy)].

[36] X. Antoine, A. Levitt, and Q. Tang, *Journal of Computational Physics* **343**, 92 (2017).

[37] S. Ronen, D. C. E. Bortolotti, and J. L. Bohn, *Phys. Rev. A* **74**, 013623 (2006).

[38] Janner, A., Janssen, T., and de Wolff, P.M., *Europhys. News* **13**, 1 (1982).

[39] D. Baillie and P. B. Blakie, *Phys. Rev. Lett.* **121**, 195301 (2018).

[40] A. J. Leggett, *Phys. Rev. Lett.* **25**, 1543 (1970).

[41] N. Sepúlveda, C. Josserand, and S. Rica, *Phys. Rev. B* **77**, 054513 (2008).

[42] S. Ostermann, V. Walther, and S. F. Yelin, *Phys. Rev. Research* **4**, 023074 (2022).

[43] S. M. Roccuzzo, S. Stringari, and A. Recati, *Phys. Rev. Research* **4**, 013086 (2022).

[44] Y. Guo, R. M. Kroeze, B. P. Marsh, S. Gopalakrishnan, J. Keeling, and B. L. Lev, *Nature* **599**, 211 (2021).

[45] Note that within our current model, which neglects propagation effects in the Helmholtz equation, the usual thermodynamic limit  $N \rightarrow \infty, L \rightarrow \infty$  and finite  $N/L$  leads to diverging energy [10, 34], on the one hand. While on the other hand, the modified thermodynamic limit  $L \rightarrow \infty$  with finite  $N$  [10] nullifies the effect of dipole and contact interactions.

[46] C. Mishra, S. Ostermann, F. Mivehvar, and B. Prasanna Venkatesh, (In Preparation).

[47] D. A. Steck, *Quantum and Atom Optics* (available online at <http://steck.us/teaching> (revision 0.12.2, 11 April 2018), ).

[48] M. Lu, S. H. Youn, and B. L. Lev, *Phys. Rev. A* **83**, 012510 (2011).

## Supplemental Material

### VARIATIONAL EXTENDED GROSS-PITAEVSKII EQUATION COUPLED TO LIGHT

For the sake of completeness, we provide details of the variational extended Gross-Pitaevskii equation (eGPE) coupled to light fields [Eq. (1-3) in the main text] here. The equation for the axial order parameter  $\psi(z)$  is given by:

$$i\hbar \frac{\partial \psi(z, t)}{\partial t} = \left[ \mathcal{E}_p - \frac{\hbar^2 \nabla_z^2}{2m} + V(z) + \frac{gN}{2\pi l^2} |\psi|^2 + \Phi_p(z) + N^{3/2} g_{\text{LHY}} |\psi|^3 \right] \psi(z, t). \quad (\text{S1})$$

This equation has to be solved in conjunction with the minimisation of the following energy functional with respect to the parameters  $l, \eta$  that determine the full 3D order parameter  $\Psi(\mathbf{r}, t) = \psi(z, t) e^{-(\eta x^2 + y^2)/2l^2} / \sqrt{\pi l}$ :

$$\mathcal{E}(\psi; l, \eta) = \mathcal{E}_p + \int dz \psi^*(z, t) \left[ -\frac{\hbar^2}{2m} \nabla^2 + V(z) + \frac{gN}{4\pi l^2} |\psi|^2 + \frac{\Phi_p}{2} + \frac{2g_{\text{LHY}} N^{3/2}}{5} |\psi|^3 \right] \psi(z, t). \quad (\text{S2})$$

As mentioned in the main text, we numerically solve Eq. (S1) for a given realization of the light-induced potential  $V_{\text{opt}}(z) = -\alpha(|E_L(z)|^2 + |E_R(z)|^2)$ . The governing Helmholtz equation for the light fields that determine the optical potential is given as:

$$\frac{\partial^2}{\partial z^2} E_{L,R}(z) + \frac{(2\pi)^2}{\lambda_0^2} \left[ 1 + \zeta \lambda_0 |\psi(z, t)|^2 \right] E_{L,R}(z) = 0, \quad (\text{S3})$$

and is solved together with Eq. (S1). We next describe the method used to solve the Helmholtz equation [S10].

### HELMHOLTZ EQUATION SOLUTION

We now detail the procedure to solve the Helmholtz equation [Eq. (S3)] for a given condensate order parameter  $\psi(z, t)$  inside the finite sized box potential extending from  $-L/2 < z < L/2$ . Consider the incident beam on the BEC of size  $L$  from left. The boundary conditions to solve the Helmholtz equation for either the left or the right propagating light field within the BEC can be determined by first recognizing that the light field to the left of the condensate is given by  $E^{\text{left}}(x) = A e^{ik_0(x+L/2)} + B e^{-ik_0(x+L/2)}$  and field to the right denoted by  $E^{\text{right}}(x) = D e^{ik(x-L/2)}$  [S10]. The relation between the incident ( $A$ ), reflected ( $B$ ), and transmitted ( $D$ ) amplitudes is given by:

$$B = r_c A \quad (\text{S4})$$

$$D = t_c A \quad (\text{S5})$$

and defines the reflection and transmission coefficients  $r_c$  and  $t_c$  respectively. Note that  $|r_c|^2 + |t_c|^2 = 1$ . The electric field at the boundary of the BEC is given by:

$$\begin{aligned} E^{\text{left}}(-L/2) &= A + B, & \frac{\partial E^{\text{left}}}{\partial z}(-L/2) &= ik_0(A - B), \\ E^{\text{right}}(L/2) &= D, & \frac{\partial E^{\text{right}}}{\partial z}(L/2) &= ik_0 D. \end{aligned} \quad (\text{S6})$$

In order to compute  $r_c$  we take an arbitrary value for the incident amplitudes  $E^{\text{left}}(-L/2)$  and  $\frac{\partial E^{\text{left}}}{\partial z}(-L/2)$ , as the Cauchy boundary condition and solve the Helmholtz equation in the region  $-L/2 \leq z \leq L/2$  using the fourth order Runge-Kutta method. This allows us to determine  $E^{\text{right}}(L/2)$  and  $\frac{\partial E^{\text{right}}}{\partial z}(L/2)$ . From the ratios  $r_1 = E^{\text{left}}(-L/2)/E^{\text{right}}(L/2)$  and  $r_2 = \dot{E}^{\text{left}}(-L/2)/\dot{E}^{\text{right}}(L/2)$  (where  $\dot{E} = \frac{\partial E}{\partial z}$ ), one obtains the reflection coefficient as

$$r_c = \frac{r_1 - r_2}{r_1 + r_2}, \quad (\text{S7})$$

for a given atomic order parameter  $\psi(z, t)$ . Once we have  $r_c$ , we can now set the amplitude of the incident light as the laser driving field amplitude  $A = E_0$  and solve the Helmholtz equation with boundary conditions given by Eqs. (S4)-(S6) to determine  $E_L(z)$ . A similar approach can be used to solve for  $E_R(z)$  using the light beam incident from the right. Since we have only considered symmetric driving strength from the left and right, we will get the same  $r_c$  for both cases.

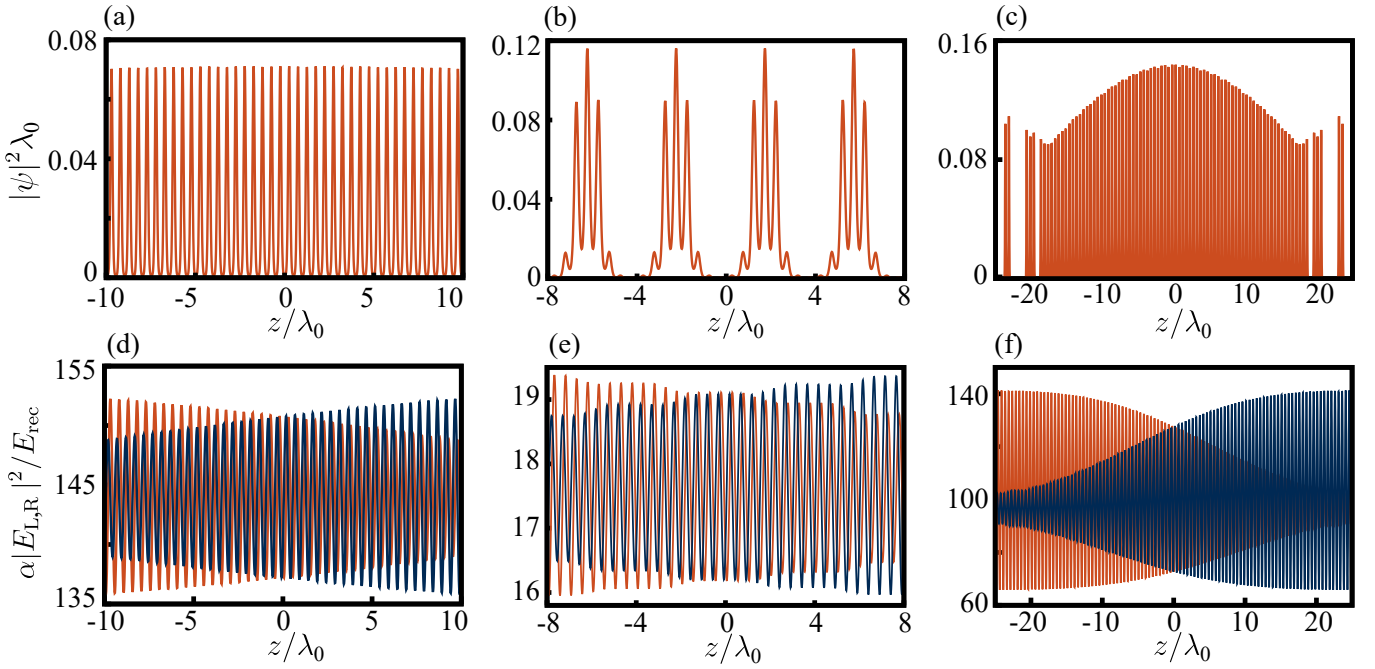


Figure S1. (a-b) Density profiles shown in Fig. 1(d-e) respectively. (c) Density profile corresponding to  $\{g_d/g, \sqrt{\alpha}E_0/E_{\text{rec}}\} = \{1.7, 10\}$  with all other parameters the same as in Fig. 1. The bottom row (d-f) depicts the light field intensity profiles corresponding to (a-c) respectively obtained from the solution of the Helmholtz equation.

As an example, in Fig. S1 we plot densities and their corresponding left and right propagating light fields corresponding to Figs. 1(d-e) from the main text and for a region with both strong LII and DDI [Fig. S1(c)]. The development of a periodic potential breaking the translation symmetry of the light field intensity accompanying the development of the periodic crystalline structures for the atomic density is clearly shown. One feature to note in Fig. S1 is that in general we find that the peak intensity of the standing-wave light monotonically decreases (in the direction of propagation of the applied travelling wave) in a region with an atomic density wave. Interestingly, this feature helps one to also identify gaps between atomic density waves as in Fig. S1(b,e) by noticing that the peak intensity is preserved in ‘atomic grating’ free regions.

### EXCITATION SPECTRUM

The dimensionless eGPE and Helmholtz equation, scaled using recoil energy  $E_{\text{rec}} = \hbar^2 k_0^2 / 2m$  for a homogeneous condensate of size  $L$  reads as,

$$i \frac{\partial}{\partial \tilde{t}} \tilde{\psi}(z, t) = \left[ -\frac{1}{(2\pi)^2} \frac{\partial^2}{\partial \tilde{z}^2} - (|\tilde{E}_L(z)|^2 + |\tilde{E}_R(z)|^2) + \tilde{g}(l)|\psi|^2 + \tilde{g}_d(l) \int \frac{d\tilde{k}_z}{2\pi} e^{i\tilde{k}_z \tilde{z}} \tilde{n} V_d(\tilde{k}_z) + \tilde{g}_{\text{LHY}}(l) |\psi|^3 \right] \psi(z, t), \quad (\text{S8})$$

$$\frac{\partial^2}{\partial \tilde{z}^2} \tilde{E}_{L,R}(z) + (2\pi)^2 [1 + \zeta |\tilde{\psi}(z, t)|^2] \tilde{E}_{L,R}(z) = 0, \quad (\text{S9})$$

where  $\tilde{z} = z/\lambda_0$ ,  $\tilde{k}_z = k_z \lambda_0$  and  $\tilde{t} = t \omega_{\text{rec}}$ . We have used  $\tilde{g} = gN/(2\pi l_\rho^2 \lambda_0 E_{\text{rec}})(l_\rho^2/l^2)$ ,  $\tilde{g}_d = g_d N/(2\pi l_\rho^2 \lambda_0 E_{\text{rec}})(l_\rho^2/l^2)$ ,  $\tilde{g}_{\text{LHY}} = N^{3/2} g_{\text{LHY}}/E_{\text{rec}} \lambda_0^{3/2}$ , and  $\tilde{E}_{L,R} = \sqrt{\alpha/E_{\text{rec}}} E_{L,R}$ . As mentioned in the main text, we consider the following ansatz for plane wave excitations about homogeneous solutions  $\psi_0(z) = 1/\sqrt{L}$  and  $E_{L,R}^0(z) = E_0 e^{\pm i k_{\text{eff}} z}$ :

$$\begin{aligned} \tilde{\psi}(z) &= [\tilde{\psi}_0(z) + u e^{-i(\tilde{k}_z \tilde{z} - \tilde{\omega} \tilde{t})} + v^* e^{i(\tilde{k}_z \tilde{z} - \tilde{\omega} \tilde{t})}] e^{-i\mu \tilde{t}}, \\ \tilde{E}_{L,R}(z) &= \tilde{E}_{L,R}^0(z) + \delta E. \end{aligned}$$

We use the above ansatzes in Eqs. (S8)-(S9) and consider terms up to linear order in the fluctuations  $\delta E, u, v^*$ . The calculations are easily performed in Fourier space. After reverting back to position space, we obtain,

$$\delta E = -(2\pi)^2 \zeta \frac{1}{\sqrt{L}} \tilde{E}_0 \left[ \frac{(u + v) e^{-i(\tilde{k} + \tilde{k}_{\text{eff}}) + i\tilde{\omega} \tilde{t}}}{\tilde{k}_{\text{eff}}^2 - (\tilde{k} + \tilde{k}_{\text{eff}})^2} + \frac{(u^* + v^*) e^{i(\tilde{k} - \tilde{k}_{\text{eff}}) - i\tilde{\omega} \tilde{t}}}{\tilde{k}_{\text{eff}}^2 - (\tilde{k} - \tilde{k}_{\text{eff}})^2} \right]. \quad (\text{S10})$$

Using Eq. (S10) along with the ansatz in Eq. (S8), the eGPE is linearized in a standard way to arrive at the following dispersion relation,

$$\epsilon(\tilde{k}_z)^2 = \frac{\tilde{k}_z^2}{(2\pi)^2} \left[ \frac{\tilde{k}_z^2}{(2\pi)^2} - \frac{8(2\pi)^2 \zeta \tilde{E}_0^2}{\tilde{L}(\tilde{k}_z^2 - 4\tilde{k}_{\text{eff}}^2)} + \frac{2\tilde{g}}{\tilde{L}} + \frac{2\tilde{g}_d}{\tilde{L}} V_d(\tilde{k}_z) + \frac{3\tilde{g}_{\text{LHY}}}{\tilde{L}^{3/2}} \right], \quad (\text{S11})$$

which is the dimensionless version of Eq. (4) of the main text. Note that  $\tilde{g}$ ,  $\tilde{g}_d$ , and  $\tilde{g}_{\text{LHY}}$  depend on the the variational parameters  $l$  and  $\eta$ , which are obtained from a minimization of the following reduced form of Eq. (S2),

$$\mathcal{E}_{\text{hom}} = \left( \frac{1}{8\pi\tilde{l}^2} + \frac{\tilde{l}^2}{8\pi^2\tilde{l}_\rho^4} \right) \left( \eta + \frac{1}{\eta} \right) + \frac{\tilde{g}(l)}{\tilde{L}} + \frac{\tilde{g}_d(l)}{\tilde{L}} \left( \frac{3}{1+\eta} - 1 \right) + \frac{2}{5} \frac{\tilde{g}_{\text{LHY}}}{\tilde{L}^{3/2}} - 2\tilde{E}_0^2. \quad (\text{S12})$$

## INITIAL GUESSES

The different initial guesses used to obtain Fig. 2 of the main text are either multigaussian ( $\psi_{\text{Gaussian}}$ ), Tanh ( $\psi_{\text{Tanh}}$ ) or Thomas-Fermi ( $\psi_{\text{TF}}$ ) profiles, where

$$\begin{aligned} \psi_{\text{Gaussian}} &= \mathcal{A}_{\text{Gaussian}} \sum_{i=1}^v e^{-\frac{(z-z_i)^2}{2\sigma^2}}, \\ \psi_{\text{Tanh}} &= \mathcal{A}_{\text{Tanh}} \sqrt{\tanh(z+\sigma) - \tanh(z-\sigma)}, \\ \psi_{\text{TF}} &= \mathcal{A}_{\text{TF}} \sqrt{1 - \frac{z^2}{\sigma^2}}. \end{aligned}$$

The pre-factor  $\mathcal{A}_j$  for  $j \in [\text{Gaussian}, \text{Tanh}, \text{TF}]$  are normalization constants and  $\sigma$  is proportional to the spatial widths. In case of multigaussian ansatzes we have used cases with  $6 \leq v \leq 10$  and  $\sigma/\lambda_0 \sim 2$ . For Tanh and Thomas-Fermi ansatzes  $\sigma$  has been chosen such that  $|\psi_{\text{Tanh}, \text{TF}}|^2$  spans the entire numerical box width.

In the LMC phase, the energy landscape consists of numerous local minima around the global minima for strong DDI. For  $S$  different ansatzes listed above, solutions converge to qualitatively similar yet quantitatively different ground states with  $P$  different energy values ( $E_p$  with  $p \in P$ ) where  $P \leq S$ . We employ the parameter  $\Delta E = |E_p^{\text{max}} - E_p^{\text{min}}|$ , the span between the maximum and minimum energy obtained from  $S$  different initial guesses, to characterize the non-convexity of the energy landscape. We have used  $S = 6$  for Fig. 2.

## HEATING RATE CALCULATION

The frequency dependent polarizability of a two level atom subject to a light field with detuning  $\Delta_a$  is given by [for  $\Delta_a \gg \Gamma$  with  $\Gamma$  denoting the linewidth (spontaneous emission rate) of the transition] [S47],

$$\alpha(\omega) = \frac{\alpha_0 \omega_0^2}{\omega_0^2 - \omega^2} \approx \frac{\omega_0 \alpha_0}{2\Delta_a}, \quad (\text{S13})$$

where  $\alpha_0 = 2\mu^2/\hbar\omega_0$  is the static polarizability for a transition frequency  $\omega_0$  and transition electric dipole moment  $\mu$ . Note that the light-atom coupling parameter  $\zeta = \alpha N / 2\pi\epsilon_0\lambda_0 l^2$  is determined by the polarizability  $\alpha(\omega)$ . Since in all calculations presented in the main text, we choose  $\zeta = 0.1$ , we will choose detuning  $\Delta_a$  to ensure this is satisfied. The heating rate due to spontaneous emission for atoms subject to light of intensity  $I$  is given by:

$$R = \frac{\Gamma^3}{8\Delta_a^2} \frac{I}{I_{\text{sat}}}, \quad (\text{S14})$$

with the saturation intensity  $I_{\text{sat}}$  given by

$$I_{\text{sat}} = \frac{2\pi\hbar\omega_0\Gamma}{6\lambda_0^2}, \quad (\text{S15})$$

for a two-level atom model. Focusing on Dysprosium (Dy) we find that the data for  $\Gamma$  and  $I_{\text{sat}}$  for different optical transitions are presented in Ref. [S48]. Since the dipole moment strength  $\mu$  is not directly available we estimate the same using Eq. (S15) and the expression for spontaneous emission rate of a two-level atom  $\Gamma = \omega_0^3 \mu^2 / (3\pi\epsilon_0 \hbar c^3)$  as:

$$\mu = \sqrt{\frac{c\epsilon_0 \hbar^2 \Gamma^2}{4I_{\text{sat}}}},$$

with  $c$  and  $\epsilon_0$  denoting the speed of light and permittivity of free space. Choosing the  $\lambda_0 = 741\text{nm}$  transition in Dy with  $I_{\text{sat}} = 0.57\text{ }\mu\text{W/cm}^2$  and  $\Gamma = 1.12 \times 10^4\text{ Hz}$  [S48], we find that a detuning of  $\Delta_a \sim 2\pi \times 1.6\text{MHz}$  leads to  $\zeta = 0.1$  for our chosen system parameters with  $N = 10^5$  atoms confined in a transverse trap  $\omega_\rho/2\pi = 100\text{Hz}$ . Note that we use the transverse trap frequency to estimate the cross-section as  $l^2 \sim l_\rho^2 = \hbar/(m\omega_\rho)$  in the expression of  $\zeta$ . This leads to the estimate of the heating rate of  $R \sim 34\text{Hz}$  presented in the main text. For the sake of completeness and to show that there is enough room in terms of choice of experimental parameters, we first present below a table giving the detuning  $\Delta_a$  choices and heating rates for different lines of Dy with  $(N, A \equiv 2\pi l_\rho^2) = (10^5, 4 \times 10^{-12}\text{m}^2)$ :

$\lambda_0(\text{nm})$	$I(\text{W/m}^2)$	$\Gamma(\text{Hz})$	$\mu(\text{Debye})$	$\alpha (\text{Hz}\cdot\text{cm}^2/\text{V}^2)$	$\Delta_a(\text{MHz})$	$R(\text{Hz})$
1001	$3 \times 10^3$	330	0.032	265h	0.5	20
741	$4.4 \times 10^3$	$1.12 \times 10^4$	0.12	370h	10	34
626	$5 \times 10^3$	$8.5 \times 10^5$	0.81	337h	500	52
598	$5 \times 10^3$	$7.7 \times 10^4$	0.22	332h	50	59
421	$7.3 \times 10^3$	$2 \times 10^8$	6.93	221h	$5.5 \times 10^4$	113

In a similar manner we also find the following possibilities for Erbium (Er) with  $(N, A) = (5 \times 10^5, 4 \times 10^{-12}\text{m}^2)$  in all cases:

$\lambda_0(\text{nm})$	$I(\text{W/m}^2)$	$\Gamma(\text{Hz})$	$\mu(\text{Debye})$	$\alpha (\text{Hz}\cdot\text{cm}^2/\text{V}^2)$	$\Delta_a(\text{MHz})$	$R(\text{Hz})$
1299	$1.1 \times 10^4$	5.6	0.006	142	0.07h	6
841	$1.7 \times 10^4$	$5 \times 10^4$	0.3	93	250h	6
631	$1.8 \times 10^4$	$1.8 \times 10^5$	0.37	91	400h	13
582	$1.8 \times 10^4$	$1 \times 10^6$	0.77	90	1700h	18
400	$1.7 \times 10^4$	$1.7 \times 10^8$	5.85	91	95000	55